RSC Advances

PAPER

View Article Online
View Journal | View Issue

Cite this: *RSC Adv.*, 2026, **16**, 6960

Hypophosphite-assisted ball milling enables broadband self-trapped exciton emission in copper halides for self-powered smart windows

Yuan Xie,† Jingyu Zhang,† Bocong Zhang, Jie Liu, Junhui Ding, Tianyu Gao, Anhong Chen, Wanqiu Wang, Yisi Wang and Aifei Wang *

Metal halide perovskites have shown remarkable potential in photovoltaic and optoelectronic applications due to their excellent light absorption, high defect tolerance, and long carrier diffusion lengths. In this study, we systematically investigate copper-based metal halides and introduce a hypophosphorous acid-assisted mechanochemical ball milling strategy to construct highly stable copper halide systems. Leveraging the broadband emission characteristics of self-trapped excitons (STE), we explore the controlled synthesis and optoelectronic applications of these materials. Using $DPCu_4Br_6$ (DP = *p*-phenylenediamine) as a representative compound, we achieved outstanding optical performance, including broadband emission (FWHM = 120 nm), minimal reabsorption, ultrahigh photoluminescence quantum yield (PLQY = 98.38%), and a long exciton lifetime of 47.62 μs. Remarkably, the material retained over 80% of its PLQY after six months of exposure to ambient air, demonstrating superior environmental stability. Based on these results, a 6 × 6 cm^2 luminescent solar concentrator (LSC) was fabricated, achieving an optical conversion efficiency (η_{opt}) of 12.43%, and successfully integrated with electrochromic smart windows to enable self-powered light modulation through a synergistic system design.

Received 29th October 2025
Accepted 23rd January 2026

DOI: 10.1039/d5ra08298f

rsc.li/rsc-advances

Introduction

Fluorescent solar concentrators (LSCs), which can be fabricated as transparent or semi–transparent devices, have attracted considerable attention due to their potential applications in building-integrated photovoltaics, smart windows, net–zero energy buildings, and space solar power systems.[1–3] Their working principle relies on fluorescent materials embedded in a transparent substrate that absorb sunlight and re-emit photons. The emitted light is guided by total internal reflection toward the edges of the substrate, where it is collected by the attached solar cells for power generation. This design reduces the required area of photovoltaic panels, lowers costs, and enables device transparency. The efficiency of LSCs is primarily determined by the properties of the fluorescent materials within the transparent matrix. Ideally, such materials should exhibit a large absorption coefficient, high PLQY, and minimal reabsorption, thereby enhancing solar concentration while suppressing self-absorption and quenching losses.[4]

In recent years, metal halide semiconductors have attracted significant attention in the academic community due to their unique physical and chemical properties.[5,6] Compared with traditional semiconductor-based fluorescent materials, these compounds offer distinct advantages. First, they exhibit excellent optical properties, including a broad spectral absorption range, a tunable bandgap structure, and an unusual tolerance to lattice defects, all of which contribute to high PLQY.[7] Second, they can be processed easily at low temperatures, rely on abundant raw materials, and are cost-effective, making them ideal candidates for LSC fluorescent materials. However, the best–performing metal halide materials in terms of optical properties remain lead-based perovskites, whose inherent toxicity and poor environmental stability pose major obstacles to industrial applications. Lead (Pb^{2+}) is highly mobile in the environment and prone to bioaccumulation, raising serious health concerns.[8] The World Health Organization (WHO) classifies lead compounds as Group 2A carcinogens.[9] These challenges have prompted researchers to explore environmentally friendly, lead-free metal halide systems. The central issue in developing such systems lies in balancing environmental safety with the preservation of favorable material properties through elemental substitution and structural design. Current research strategies mainly focus on incorporating low-toxicity metal cations such as tin (Sn^{2+}),[10,11] copper (Cu^{+}),[12] and antimony (Sb^{3+}).[13] Among them, copper(I)–based halides have demonstrated remarkable potential for optoelectronic applications due to their facile synthesis, high absorption coefficients, low cost, excellent fluorescence quantum yields, and environmental compatibility.[14–16] To address these challenges, we propose

State Key Laboratory of Flexible Electronics (LoFE), Institute of Advanced Materials (IAM), School of Flexible Electronics (Future Technologies), Nanjing Tech University (NanjingTech), Nanjing 211816, Jiangsu, China

† Yuan Xie and Jingyu Zhang contributed equally to this work.

a mechanochemical synthesis route to prepare the copper–based halide system $DPCu_4X_6$ (DP = *p*-phenylenediamine, X = Br^-, I^-) *via* a hypophosphorous acid-assisted ball milling method, enabling large-scale and controllable material production. The resulting compounds exhibit a PLQY of 98.38%, efficient luminescence without reabsorption, and excellent environmental stability. When employed as fluorescent fillers in LSC devices, they were used to fabricate highly transparent power–generating glass, which was further integrated with electrochromic glass to realize self-powered electrochromic functionality.

Materials & methods

Materials

Copper bromide (CuBr, mass fraction ≥99.9%), cuprous iodide (CuI, mass fraction ≥99.9%), Shanghai McLean Biochemical Technology Co., Ltd ; H_3PO_2 (mass fraction ≥50%, aqueous solution), Shanghai Aladdin Biochemical Technology Co., Ltd ; *p*-phenylenediamine (DP, mass fraction ≥99%), Sinopharm Chemical Reagent Co., Ltd ; isopropyl alcohol (mass fraction ≥99.9%), Merck Group; bis (trifluoromethylsulfonyl) imide heptyl amethyst (mass fraction ≥99.99%), propylene carbonate (PC, mass fraction ≥99.95%), ferrocene (mass fraction ≥ 99.99%), methanol (mass fraction ≥99.9%), bis (trifluoromethylsulfonyl) imide lithium salt (mass fraction ≥98%), polyvinyl butyral (PVB), polydimethylsiloxane (PDMS), Shanghai Bide Pharmaceutical Technology Co., Ltd ; FTO/ITO conductive glass (resistance < 15 Ω), Liaoning preferred new energy technology Co., Ltd ; photovoltaic welding strip, Tab Wire Company; ultra-white tempered glass, Luoyang Guluo Glass Co., Ltd ; silicon wafer battery, Shanghai Suiying Photovoltaic Technology Co., Ltd.

Preparation of $DPCu_4X_6$ (X = Br, I)

CuX (X = Br, I), DP, and H_3PO_2 were mixed in a molar ratio of 1 : 1:5 and loaded into a ball mill jar. The mixture was subjected to planetary ball milling for 30 min. After milling, a white emulsion was obtained, to which anhydrous ethanol was added for ultrasonic cleaning for 10 min. This washing step was repeated three times. The resulting crude solution was then centrifuged at 8000 rpm for 10 min, the supernatant was discarded, and the precipitate was dried to yield $DPCu_4X_6$ as a white powder.

Reparation of $DPCu_4Br_6$–based LSC

For LSC fabrication, 10 g of PDMS was mixed with 1 g of curing agent and degassed under vacuum until no visible bubbles remained. The synthesized $DPCu_4Br_6$ powder was dispersed in isopropanol (IPA) *via* ultrasonic treatment and then combined with the PDMS precursor through thorough stirring to form a homogeneous composite ink, which was subsequently degassed under vacuum. The ink was deposited onto 6 × 6 cm^2 ultra-clear glass substrates using an ultrasonic spray coater with a spraying area of 10 × 10 cm^2, the nozzle connected to nitrogen, and the stage heated to 100 °C under vacuum. Prior to spraying, the ink was diluted with IPA, and 10 mL of the solution was sprayed onto each substrate. The coated substrates were then subjected to vacuum hot pressing at 100 °C for 40 min. Finally, silicon solar cells were attached around the edges of the coated glass using photovoltaic welding strips to complete the LSC devices.

Preparation of self-powered color-changing glass based on $DPCu_4Br_6$

Electrochromic gel preparation. Electrochromic gel was prepared by dissolving 300 mg of polyvinyl butyral (PVB), 150 mg of polycarbonate (PC) matrix, 23 mg of ferrocene, 160 mg of lithium bis(trifluoromethylsulfonyl)imide, and 0.1 mmol of heptyl ammonium bis(trifluoromethylsulfonyl) imide in 1.5 mL of ultra-dry methanol. The solution was continuously stirred under argon protection for 180 min to obtain a homogeneous, transparent solution. The mixture was then left to undergo natural sedimentation to remove trapped gas, yielding a gel material with photochromic properties.

Electrochromic device fabrication. Electrochromic devices were prepared using a sandwich structure. A 6 × 6 cm^2 FTO glass substrate was coated with 2 mL of the electrochromic gel using a microsyringe. A second, identical FTO glass was placed on top to seal the device, forming a two-electrode configuration. The assembly was cured at room temperature for 180 s, producing a functional electrochromic layer.

Integration with LSC for self-powered operation. unlike traditional electrochromic devices, the system developed here integrates the $DPCu_4Br_6$-based luminescent solar concentrator (LSC) with the electrochromic device *via* electrode clamps. This series circuit of LSC and electrochromic component enables a light-driven, self-powered dimming system without the need for an external power supply.

Characterizations

The PL and PLE spectra were collected by a fluorescence spectrometer (HITACHI F-7100). Photoluminescence quantum yields (PLQY), time-resolved (transient photoluminescence spectroscopy), and temperature-dependent PL spectra tests were performed using a fluorescence 7 spectrometer (Edinburgh Instruments FLS980) equipped with an integrated sphere under ambient conditions. Absorption spectra were measured by a UV-visible near-infrared spectrophotometer (PerkinElmer, PE Lambda 950). Surface roughness was measured by a Park atomic force microscope (Park, XE-70). X-ray diffraction (XRD) analysis was carried out on Smartlab-4 using Cu Kα radiation (λ = 1.5406 Å), and the diffraction pattern was scanned over the angular range of 10–50° (2θ) at room temperature. Transmission electron microscope (SEM) images were recorded on a JEM-1400PLUS (JEOL Ltd, 200 kV). *J–V* curves were measured by solar simulator inch (SS–F5-3A, Enlitech) under AM 1.5 G standard light. The incident photon-to-electron conversion efficiency (IPCE) measurements were carried out by a QE-R-900AD system (Nanjing Ouyi Optoelectronics Technology).

Results and discussion

Unlike solution-based methods, which are limited by solvent toxicity and scalability, solvent-free ball milling offers a readily scalable synthesis route. Initial attempts to prepare copper halides using only cuprous halides (CuX) and *p*-phenylenediamine (DP) produced black powders under ambient light. Under 365 nm UV excitation, only the characteristic fluorescence of unreacted DP was observed (Fig. 1), indicating that no reaction occurred during milling. Successful synthesis was achieved by introducing hypophosphorous acid (H_3PO_2). As shown in Fig. 1, incremental additions of H_3PO_2 (100–300 μL) progressively shifted the powder color from dark to white under daylight, while bright yellow fluorescence appeared under UV illumination. This dose-dependent transformation demonstrates that H_3PO_2 effectively prevents Cu^+ oxidation and suppresses defect formation, including Br vacancies.

Systematic investigation of precursor stoichiometry revealed a strong dependence of luminescence performance on the CuBr : DP molar ratio. At a 2 : 1 ratio, the product exhibited intense yellow emission centered at 554 nm (Fig. 2a), red-shifted by 3 nm and significantly enhanced in intensity compared with the 1 : 1 counterpart. Halogen substitution was then achieved by replacing bromine with iodine under identical mechanochemical conditions, yielding $DPCu_4I_6$. The crystalline quality of both $DPCu_4Br_6$ and $DPCu_4I_6$ was confirmed by X-ray diffraction (XRD), with peak positions precisely matching reference patterns (CCDC No. 2236273 and 2253788) and no impurity peaks observed (Fig. 2b).[17] The flat baseline, sharp Gaussian peak profiles, and absence of anomalies collectively indicate high crystallinity and phase purity.

Three-dimensional excitation–emission matrix (3D EEM) spectroscopy revealed broadband emission in both compounds. $DPCu_4Br_6$ exhibited emission spanning 480–650 nm under 320–390 nm excitation, with optimal excitation at 350 nm (Fig. 2c), whereas $DPCu_4I_6$ exhibited an extended excitation window (320–400 nm) and detectable emission under 400–430 nm excitation (Fig. 2d), consistent with triplet cluster-centered (3CC) states.[17] Both compounds display broad emission (FWHM ≈ 115 nm) and large Stokes shifts (>130 nm), ensuring negligible self-absorption. Photophysical measurements further highlight their performance. Time-resolved photoluminescence (TRPL) shows single-exponential decay lifetimes of $\tau \approx 24.71$ μs for $DPCu_4I_6$ and $\tau \approx 47.62$ μs for $DPCu_4Br_6$ (Fig. 2e), indicating lower defect density in $DPCu_4Br_6$. Under 365 nm excitation (Fig. 2f), $DPCu_4Br_6$ and $DPCu_4I_6$ exhibit high PLQY of 98.1% and 86%, demonstrating strong potential for high-efficiency LSC applications.

$DPCu_4Br_6$ exhibits superior stability, retaining a high PLQY of 80% after six months, whereas $DPCu_4I_6$ retains only 40% (Fig. 3a). Therefore, $DPCu_4Br_6$ was selected as the candidate for luminescent solar concentrator (LSC) studies. Scanning electron microscopy (SEM) characterization of $DPCu_4Br_6$ reveals irregular block-like to near-spherical agglomerates (Fig. 3b), with a mean particle diameter of 0.46 ± 0.02 μm. The thermal decomposition behavior, determined from thermogravimetric analysis (TGA) and differential scanning calorimetry (DSC), is shown in Fig. 3c. A 5% weight loss is observed at 200 °C, indicating the onset of decomposition. The DSC curve displays a small endothermic peak at 179 °C, which may correspond to local structural relaxation or weak bond cleavage (*e.g.*, intermolecular van der Waals interactions or partial Br^- coordination adjustment). A sharp and intense exothermic peak at 185 °C corresponds to the primary phase transition, without interference from overlapping or broad peaks, suggesting high crystal phase purity in the synthesized material. Temperature-dependent photoluminescence (PL) spectroscopy (Fig. 3d) of ball-milled $DPCu_4Br_6$ shows monotonic narrowing of the emission linewidth (FWHM decrease) upon cooling, characteristic of reduced electron–phonon coupling.[18] Arrhenius analysis (Fig. 3e) yields an exciton binding energy (E_a) of 122.16 meV,[19] which exceeds the thermal energy at room temperature (≈26 meV). This large binding energy indicates exceptional exciton stability against thermal dissociation, enabling intense fluorescence at ambient conditions. Furthermore, spectral fitting reveals a Huang–Rhys factor (S) of 17.28 (Fig. 3f),[20] confirming strong electron–phonon coupling consistent with efficient self-trapped exciton (STE) formation.

Leveraging the superior optical properties of $DPCu_4Br_6$, the material was mixed with a PDMS binder and spray-coated onto ultra-clear glass to form the luminescent layer for luminescent solar concentrators (LSC). Fig. 4a and b show the LSC device (6 × 6 × 1 cm) under daylight and UV lamp illumination, respectively. The device exhibits high transparency under

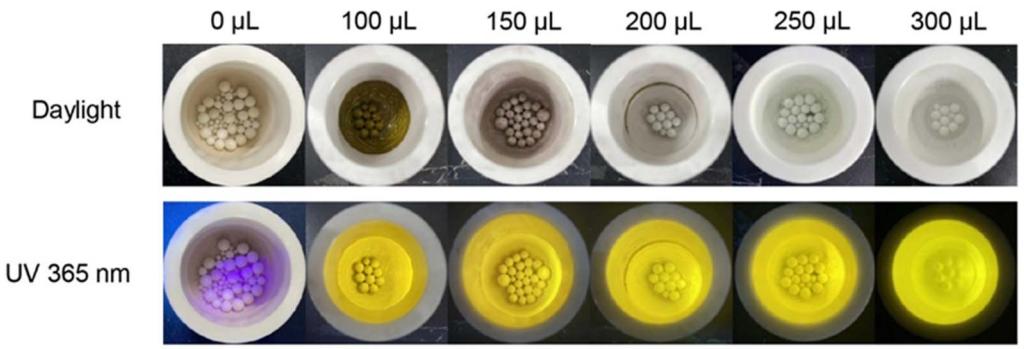

Fig. 1 Photographs of $DPCu_4Br_6$ synthesized with different hypophosphite dosages under daylight and UV (365 nm) illumination.

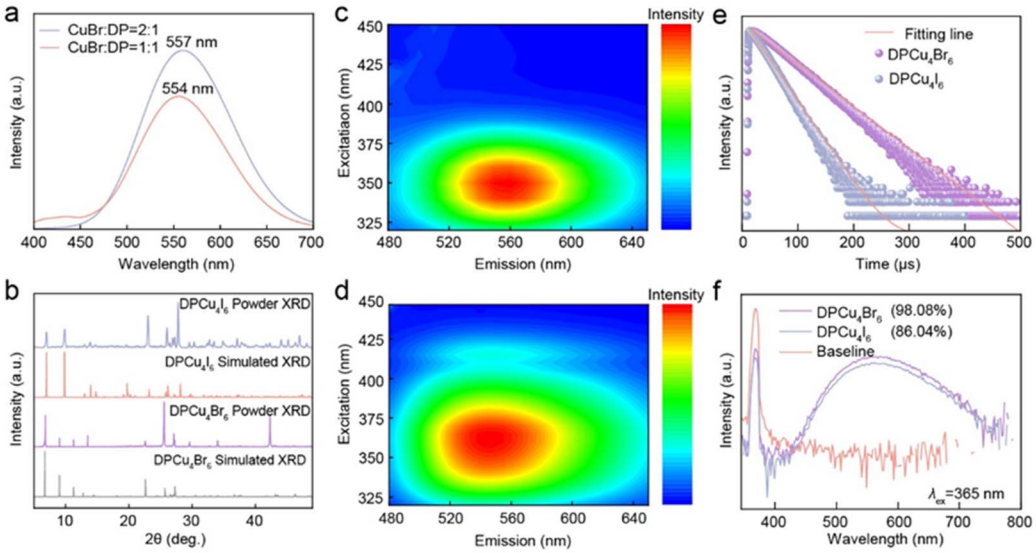

Fig. 2 (a) PL emission profiles of CuBr *versus* DP at different molar ratio. (b) X-ray diffraction (XRD) patterns of $DPCu_4Br_6$ and $DPCu_4I_6$ powders compared with standard reference cards. (c) 3D fluorescence emission spectra of $DPCu_4Br_6$ under different excitation wavelengths. (d) 3D fluorescence emission spectra of $DPCu_4I_6$ under different excitation wavelengths. (e) Time-resolved photoluminescence (TRPL) profiles. (f) PLQY measurements.

daylight conditions, while its edges display intense yellow fluorescence under UV excitation. Photoluminescence excitation (PLE) and emission (PL) spectra were recorded for the $DPCu_4Br_6$-based LSC. A distinct PLE peak is observed at ~360 nm, and a prominent PL peak appears at ~560 nm (Fig. 4c), consistent with previous PLE/PL measurements of $DPCu_4Br_6$ powder. The large Stokes shift results in negligible spectral overlap between excitation and emission bands. To evaluate reabsorption suppression, edge-waveguided PL spectra were measured at varying distances between the excitation source and the LSC. As shown in Fig. 4d, when the excitation source is placed 6 cm from the LSC, the PL peak position remains unchanged and the PL intensity is ~60% of that measured at 2 cm. This demonstrates efficient photon transport through the $DPCu_4Br_6$-based LSC waveguide. Fig. 4e presents the edge PLQY of $DPCu_4Br_6$ obtained from integrating sphere measurements, and the optical loss is further evaluated by the edge coupling efficiency (η_{edge}). The η_{edge} is as follows:

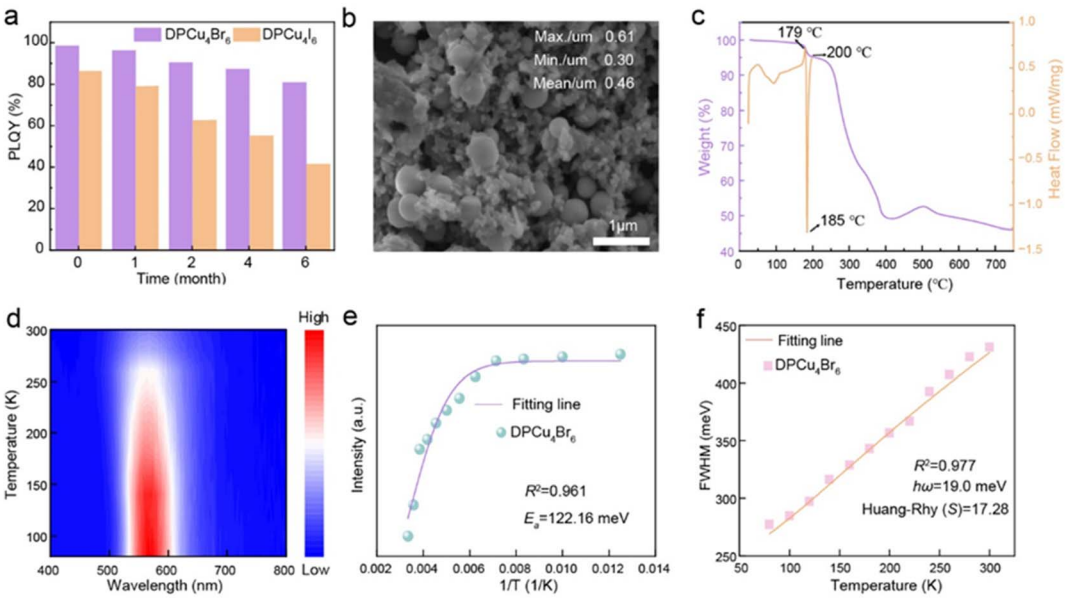

Fig. 3 (a) PLQY stability of $DPCu_4Br_6$ and $DPCu_4I_6$over time under ambient air exposure. (b) SEM images of $DPCu_4Br_6$; (c) TGA and DSC profile of $DPCu_4Br_6$. (d) Temperature-dependent fluorescence spectra of $DPCu_4Br_6$ measured from 80 to 300 K. (e) Excitation energy calculations. (f) Huang–Rhys factor calculations.

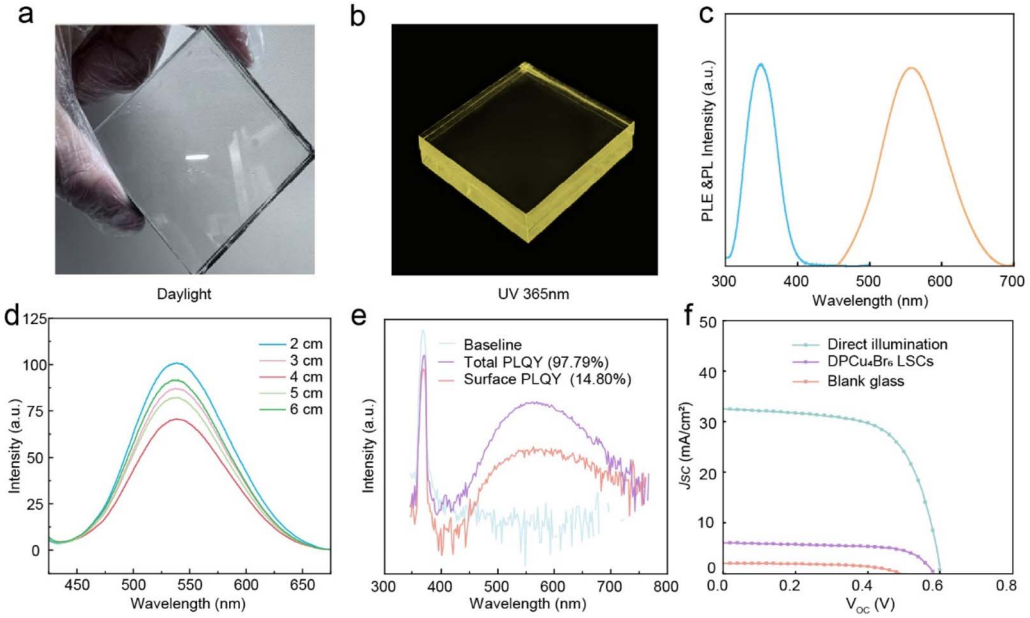

Fig. 4 (a) Photograph of the LSCs under daylight. (b) Photograph under 365 nm UV irradiation; (c) PLE and PL spectra of the LSCs. (d) Fluorescence spectra of the LSCs at different distances from the light source. (e) Surface PLQY of fabricated LSC. (f) *J*–*V* curves of $DPCu_4Br_6$.

$$\eta_{edge} = \frac{PLQY_{Total} - PLQY_{Surface}}{PLQY_{Total}} \quad (1)$$

$PLQY_{Total}$ represents the PLQY of the whole device. $PLQY_{Surface}$ is the surface PLQY measured by surrounding the device. After testing, $PLQY_{Total}$ was 97.79%, while $PLQY_{Surface}$ was 14.80%, and the η_{edge} can be obtained as 84.8%. We measure the *J-V* curves of crystalline silicon cells at the edge of the coupled and uncoupled luminescent solar concentrators. As shown in Fig. 4f, the photoelectric conversion efficiency (PCE) of the standalone crystalline silicon cell is12.67%, whereas the efficiency decreases to 2.58% when the cell is coupled to the edge of the LSC. The optical conversion efficiency (η_{opt}) is commonly

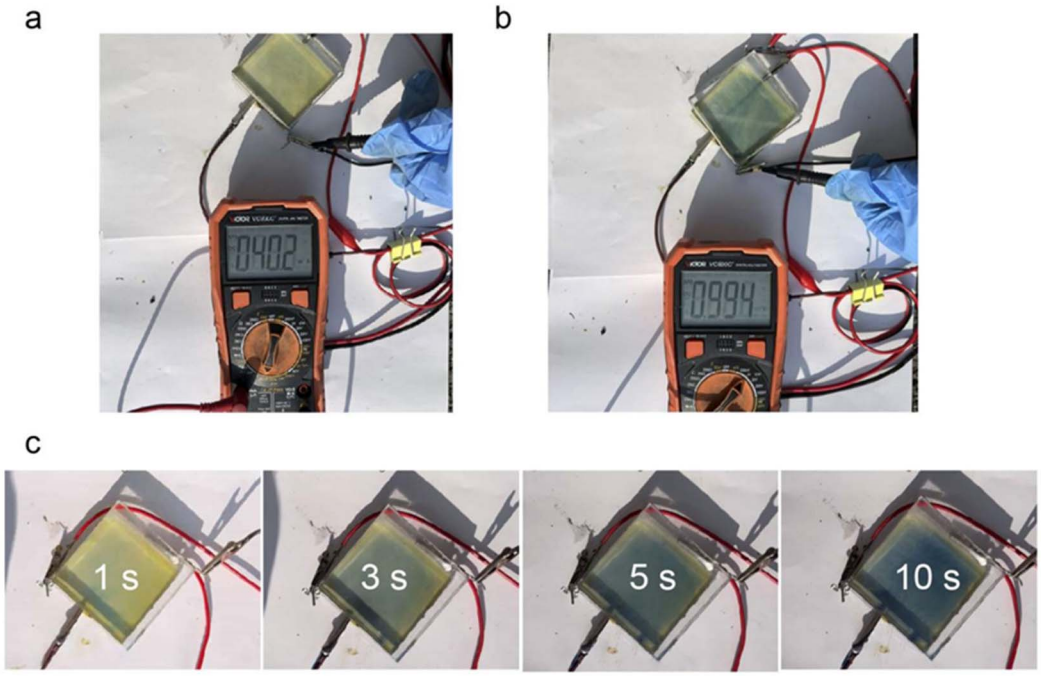

Fig. 5 (a and b) Real-time current and voltage outputs. (c) Photographs of the self-powered color-changing device exposed to daylight for 1 s, 3 s, 5 s, and 10 s.

used to evaluate the performance of LSCs, and its calculation formula is:

$$\eta_{opt} = \frac{P_{Out}}{P_{In}} = \frac{I_{LSC}}{I_{SC} \times G} \quad (2)$$

Among them, I_{LSC} represents the short-circuit current generated by the crystalline silicon cell when coupled to the LSC, while I_{SC} denotes the short-circuit current of the same cell under direct sunlight irradiation. The geometric gain factor is defined as $G = \frac{A_{front}}{A_{edge}}$. Where A_{front} is the area of incident light received by the LSC. And A_{edge} is the area of the solar cell receiving waveguide light. Based on the measured value of $G =$ 1.5 for the fully transparent photovoltaic glass sample, the optical conversion efficiency was calculated to be $\eta_{opt} = 12.43\%$.

The fabricated LSCs device functions as self-powered transparent glass and was integrated with a co-planar self-powered electrochromic device of identical dimensions. The integrated system was tested outdoors under natural sunlight to evaluate its electrochromic performance. A light-blocking mask was initially placed on the illuminated surface of the device to prevent solar irradiation. Upon rapid removal of the mask, the $DPCu_4Br_6$-based LSC generated an electrical output of 40.2 mA and 0.994 V under solar illumination (intensity: 20 000–30 000 lux; Fig. 5a and b). During prolonged exposure to sunlight, the electrochromic glass exhibited a rapid color transition from its initial tawny state to a deep blue hue. The color evolution at different exposure times is documented in Fig. 5c. These results confirm the effective solar energy harvesting and conversion capabilities of the $DPCu_4Br_6$-LSC, enabling real-time, controllable actuation of the co-integrated electrochromic device under ambient sunlight.

Conclusions

This work demonstrates a hypophosphite-assisted mechanochemical ball milling strategy for synthesizing two highly luminescent copper-based metal halides. The DPCu4Br6 compound ($DP = (C_6H_{10}N_2)_4(H_2PO_2)_6$) achieves a near-unity (PLQY = 98.38%) through efficient self-trapped exciton (STE) emission. This material also exhibits outstanding stability, with a thermal decomposition onset temperature of 200 °C and >80% PLQY retention after six months of ambient air exposure. A 6 × 6 cm^2 luminescent solar concentrator (LSC) fabricated by spray-coating $DPCu_4Br_6$ demonstrates high optical transparency and an optical conversion efficiency of 12.43%. Serial integration of this LSC with an electrochromic device enables a self-powered smart window system that achieves rapid optical switching under natural sunlight (20 000–30 000 lux). Overall, this study validates mechanochemical ball milling as a viable route for producing high-performance STE–emitting copper halides. The demonstrated LSC application potential–particularly when combined with complementary energy technologies–offers a promising pathway for building–integrated photovoltaics and contributes to the development of carbon–neutral architecture.

Author contributions

A. F. W. supervised and coordinated all aspects of this project. Y. X. carried out the synthesis and characterization, Y. X and J. Y. Z wrote the paper. B. C. Z., J. L., J. H. D., T. Y. G., A. H. C., W. Q. W, Y. S. W. measured time-resolved spectra, XRD and PLQY. A. F. W. commented on the paper, and all of the authors discussed the results.

Conflicts of interest

There are no conflicts to declare.

Data availability

The data described in the manuscript will be available upon request.

Acknowledgements

This work was supported financially by the National Natural Science Foundation of China (Grant No. 22105100).

Notes and references

1 A. Wang, J. Li, Y. Zhang, S. Cheng, Y. Wang, Y. Xie, C. Yu, H. Chen, J. Dong, J. Cao, F. Wang, W. Huang and T. Qin, *Small*, 2024, **20**, e2404149.
2 A. Wang, J. Liu, J. Li, S. Cheng, Y. Zhang, Y. Wang, Y. Xie, C. Yu, Y. Chu, J. Dong, J. Cao, F. Wang, W. Huang and T. Qin, *J. Am. Chem. Soc.*, 2023, **145**, 28156–28165.
3 J. Wang, T. Cai and O. Chen, *Nano Lett.*, 2023, **23**, 4367–4374.
4 B. S. Richards and I. A. Howard, *Energy Environ. Sci.*, 2023, **16**, 3214–3239.
5 S. Cheng, Y. Zhang, Y. Chu, Y. Wang, Y. Xie, C. Yu, J. Dong, J. Cao, F. Wang, W. Huang, A. Wang and T. Qin, *Adv. Opt. Mater.*, 2025, **13**, 2403012.
6 Z. Wang, X. Duan, J. Zhang, W. Yuan, D. Qu, Y. Chen, L. He, H. Wang, G. Yang, W. Zhang, Y. Bai and H.-M. Cheng, *Commun. Mater.*, 2024, **5**, 131.
7 C. Zhou, H. Lin, Q. He, L. Xu, M. Worku, M. Chaaban, S. Lee, X. Shi, M.-H. Du and B. Ma, *Mater. Sci. Eng. R Rep.*, 2019, **137**, 38–65.
8 M. Mukhtar, B. S. Goud, Z. Ali, M. W. Shaid, B. Naz, Q. U. Ain, M. A. Assiri, S. Sonmezoglu, A. H. Rajpar, J. H. Kim and S. Aftab, *J. Alloys Compd.*, 2025, **1026**, 180365.
9 J. Suo, H. Pettersson and B. Yang, *EcoMat*, 2025, **7**, e12511.
10 G. Vescio, D. N. Dirin, S. González-Torres, J. Sanchez-Diaz, R. Vidal, I. P. Franco, S. D. Adhikari, V. S. Chirvony, J. P. Martínez-Pastor, F. A. Vinocour Pacheco, L. Przypis, S. Öz, S. Hernández, A. Cirera, I. Mora-Seró, M. V. Kovalenko and B. Garrido, *Adv. Sustainable Syst.*, 2024, **8**, 2400060.
11 Y. Han, Z. Guo, S. Liu, Y. Wu, X. Li, G. Cui, S. Zhou and H. Zhou, *Adv. Mater.*, 2025, **37**, 2413895.

12 K.-H. Song, M. Peng, J.-J. Wang, L.-Z. Feng, Y.-C. Yin, Y.-H. Song, X.-C. Ru, Y.-P. Xie, G. Zhang, Z. Deng and H.-B. Yao, *J. Am. Chem. Soc.*, 2024, **146**, 34199–34208.
13 B. Zhuang, Z. Jin, J. Deng, H. Xiong, W. Li and J. Fan, *Adv. Opt. Mater.*, 2023, **11**, 2300888.
14 H. Peng, S. Yuan, Q. Wei, L. Kong, W. Huang, F. Wang, J. Zhao and B. Zou, *Laser Photonics Rev.*, 2025, **19**, 2401773.
15 T. Wu, Y. Shi, H. Wu, M. Chen, H. Ran, J. Zheng, X. Li, J. Chen and Y. Tang, *J. Mater. Chem. C*, 2024, **12**, 1002–1011.
16 J. Wen, K. Rong, L. Jiang, C. Wen, B. Wu, B. Sa, Y. Qiu and R. Ahuja, *Nano Energy*, 2024, **128**, 109802.
17 S. Zhou, Y. Chen, K. Li, X. Liu, T. Zhang, W. Shen, M. Li, L. Zhou and R. He, *Chem. Sci.*, 2023, **14**, 5415–5424.
18 X. Meng, S. Ji, Q. Wang, X. Wang, T. Bai, R. Zhang, B. Yang, Y. Li, Z. Shao, J. Jiang, K.-l. Han and F. Liu, *Adv. Sci.*, 2022, **9**, 2203596.
19 C. Li, S. Tscheuschner, F. Paulus, P. E. Hopkinson, J. Kießling, A. Köhler, Y. Vaynzof and S. Huettner, *Adv. Mater.*, 2016, **28**, 2446–2454.
20 Y. Jing, Y. Liu, X. Jiang, M. S. Molokeev, Z. Lin and Z. Xia, *Chem. Mater.*, 2020, **32**, 5327–5334.